

Rabi oscillations between ground and Rydberg states and van der Waals blockade in a mesoscopic frozen Rydberg gas

M Reetz-Lamour, J Deiglmayr, T Amthor and M Weidemüller

Physikalisches Institut, Universität Freiburg, Hermann-Herder-Str. 3, D-79104
Freiburg, Germany

Online at: <http://quantendynamik.physik.uni-freiburg.de>

E-mail: m.weidemueller@physik.uni-freiburg.de

Abstract. We present a detailed analysis of our recent observation of synchronous Rabi oscillations between the electronic ground state and Rydberg states in a mesoscopic ensemble containing roughly 100 ultracold atoms [M. Reetz-Lamour *et al.*, submitted, arXiv:0711.4321]. The mesoscopic cloud is selected out of a sample of laser-cooled Rb atoms by optical pumping. The atoms are coupled to a Rydberg state with principal quantum number around 30 by a two-photon scheme employing flat-top laser beams. The influence of residual spatial intensity fluctuations as well as sources of decoherence such as redistribution to other states, radiative lifetime, and laser bandwidth are analysed. The results open up new possibilities for the investigation of coherent many-body phenomena in dipolar Rydberg gases. As an example we demonstrate the van der Waals blockade, a variant of the dipole blockade, for a mesoscopic atom sample.

PACS numbers: 32.80.Ee, 37.10.De, 42.60.Jf, 32.70.Cs

1. Introduction: On aims and obstacles

Since the early days of atomic physics, atoms in highly excited electronic states (“Rydberg atoms”) have been extensively studied due to their exaggerated properties marking the borderline between classical and quantum physics [1]. Recently, Rydberg atoms have attracted interest as a possible implementation of quantum information processing based on neutral atoms [2, 3, 4, 5]. Representing an alternative to trapped ions or nuclear spins in molecular complexes [6, 7], neutral atoms offer extraordinarily weak coupling to dissipative processes of the environment thus promising long coherence times [8]. Several schemes have been proposed to entangle neutral atoms and realise quantum gates [9, 10, 3]. Ensembles of ultracold Rydberg atoms appear to be particularly promising as they exhibit controllable electric dipole interactions over

distances of many micrometres. The coherent character of these dipolar Rydberg-Rydberg interactions has been explored in ultracold gases over the last years [11, 12, 13, 14, 15] paving the way for the implementation of fast two-qubit gates.

One prominent example for the strong Rydberg-Rydberg interaction is the so-called van der Waals blockade. The van der Waals blockade is the inhibition of multiple excitations in a mesoscopic ensemble due to the interaction-induced energy shifts which separates the single excitation from multiple excitations energetically. It is a favourable tool in quantum information protocols [3] and has resulted in a number of experimental investigations. It was first observed as a suppression of excitation in macroscopic clouds for strong van der Waals interaction at high principal quantum numbers [16, 17], later for both resonant and permanent dipoles [18, 19]. It is accompanied by a change in counting statistics [20] and a modified many-body Rabi frequency which has not been observed directly so far but evidence of which has recently been found [21].

Despite this success, the realisation of single qubit operations with Rydberg atoms has proven to be particularly demanding. While stimulated adiabatic passage has been used to achieve high Rydberg excitation probabilities [22, 23], Rabi oscillations of atoms starting from the ground state are hard to observe due to the small spatial overlap between the electronic wavefunctions of ground and highly excited states resulting in very small dipole transition matrix elements. In order to achieve sufficiently high Rabi frequencies despite the small dipole matrix elements between the electronic ground state and Rydberg states, one therefore needs high laser intensities provided by tightly focussed beams. The Gaussian beam profile of a focussed laser beam, however, exhibits a wide range of intensities and would therefore impede the observation of synchronous Rabi floppings in a mesoscopic sample [23]. One may overcome this by preparing the atomic cloud in very small dipole traps, rendering the atomic cloud smaller than the excitation laser and thus only using the central part of a focussed Gaussian beam. This technique has recently been used for clouds between 1 and 10 atoms [24].

We have recently demonstrated Rabi oscillations between ground and Rydberg states in a frozen mesoscopic sample of roughly 100 ultracold atoms by applying beam shaping to ensure a constant intensity distribution over the excitation volume [25]. We restrict the excitation volume to the area where the shaped beam has a sufficiently constant intensity by spatially selective optical pumping. In this way we filter a signal of a subensemble of only 100 atoms out of a cloud of 10 million atoms. Here we discuss the experimental details and thoroughly investigate important sources of decoherence. In addition we demonstrate the van der Waals blockade for this mesoscopic system by observing a density-dependent suppression of excitation for strong van-der-Waals interaction at large principle quantum numbers n .

2. Experimental realisation

The experiment is performed with a cloud of ultracold atoms in a vapour-cell magneto-optical trap (MOT) with about 10^7 ^{87}Rb atoms at densities of 10^{10} cm^{-3} and a

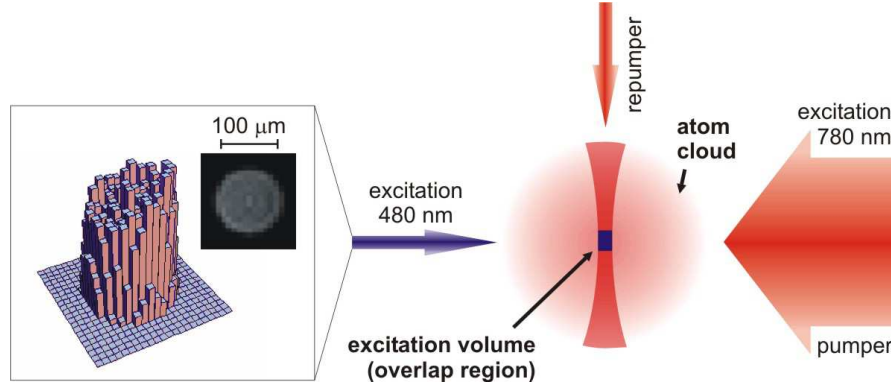


Figure 1. Preparation of a mesoscopic subensemble through spatially selective optical pumping and Rydberg excitation with a spatially homogeneous laser intensity. A small tube of atoms within a cloud of 10^7 ultracold atoms is marked by optical pumping with the pumper and repumper laser beam. A mesoscopic subensemble containing about 100 atoms within this tube is transferred to a Rydberg state by near-resonant two-photon excitation with two counter-propagating laser beams at 780 nm and 480 nm, respectively. The excitation laser at 480 nm has a flat-top intensity profile shown in the inset, while the beam at 780 nm superimposed on the pumper beam has a Gaussian profile as all other beams.

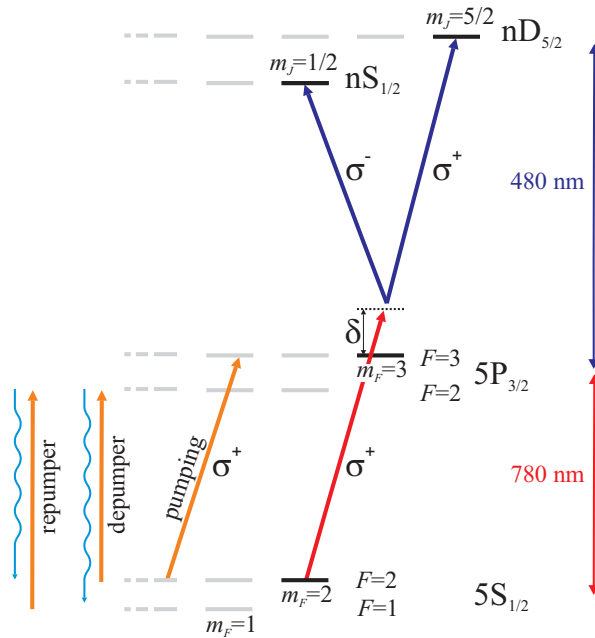


Figure 2. Level scheme for optical pumping and near-resonant two-photon excitation of ^{87}Rb Rydberg states. Addressing of a mesoscopic subset of atoms involves depumping, spatially selective repumping, and optical pumping in order to single out the 3-level subsystem $|5S_{1/2}, F=2, m_F=2\rangle \rightarrow |5P_{3/2}, F=3, m_F=3\rangle \rightarrow |n\ell_{J=\ell+1/2}, m_J=J\rangle$, with $\ell=0(\text{S})$ or $2(\text{D})$. Decoherence effects from the short lifetime of the intermediate state are minimised by the detuning δ from the intermediate resonance thereby reducing the system to an effective two-level system.

temperature below $100\ \mu\text{K}$. The excitation is achieved with two counter-propagating laser beams at $780\ \text{nm}$ and $480\ \text{nm}$ via

$$5S_{1/2} \xrightarrow{780\ \text{nm}} 5P_{3/2} \xrightarrow{480\ \text{nm}} nS_{1/2} / nD_{5/2}$$

(see Figures 1 and 2). By detuning from the intermediate state $5P_{3/2}$, this state experiences negligible population which assures sufficiently long coherence times [23]. The excitation laser at $780\ \text{nm}$ is collimated to a waist of $1.1\ \text{mm}$ ensuring a constant Rabi frequency over the excitation volume. The Rabi frequency is determined from measured Autler-Townes splittings [26, 27, 23] with typical values of $\omega/2\pi = 55\ \text{MHz}$.

The $480\ \text{nm}$ laser alignment is discussed in Sections 2.1 and 2.2. Its frequency is locked to a temperature stabilised resonator built from ZERODUR[®] which has a residual drift of $\sim 2\ \text{MHz}$ per hour. We compensate for this by repeating identical spectral measurements, determining the line centres and interpolating the resonator drift.

All lasers are switched by acousto-optical modulators (switching times $\sim 50\ \text{ns}$) and guided to the experiment by single-mode polarisation-maintaining optical fibres. This ensures an unaltered alignment independent of changes on the input side, *e.g.* when changing the laser wavelength for excitation of different Rydberg states or for different detunings from the intermediate state.

Typically $30\ \mu\text{s}$ after excitation all Rydberg atoms are field-ionised (field pulse height $770\ \text{V/cm}$) and detected with a microchannel plate detector whose signal is recorded with a boxcar integrator. The delay of $30\ \mu\text{s}$ between excitation and detection suppresses a background of “hot” ($300\ \text{K}$) atoms while it has no influence on the measured excitation probability of the cold subensemble (see Section 2.3). We have verified that no spurious ions are present which is as expected for the short timescales and small atom numbers considered throughout this article. After detection the MOT is turned back on and the whole cycle is repeated every $70\ \text{ms}$.

2.1. Beam shaping

The $480\ \text{nm}$ beam is focused and shaped to a constant intensity distribution over the excitation volume: The output of a single-mode polarisation-maintaining fibre is collimated by an achromat (focal length $80\ \text{mm}$, $1\ \text{inch}$ diameter) to a beam size ($1/e^2$ intensity radius) of $6.9\ \text{mm}$ and shaped by a diffractive optical element (DOE) which is cemented onto a plano-convex lens with a focal length of $100\ \text{mm}$ (see Fig. 3.(a)). The DOE effectively distorts the plano-convex lens to give a flattop profile at one specific distance close to the actual focus of the beam. All elements from the fibre coupler to the DOE are mounted in a rigid cage that can be aligned as a whole with respect to the MOT (see Fig. 3.(b)).

Fig. 3.(c) shows the calculated behaviour of the DOE. The flattop is realised only at one specific distance from the DOE. Before this point the beam profile is closer to a Gaussian beam, behind this point some of the beam rays cross (so-called caustics)

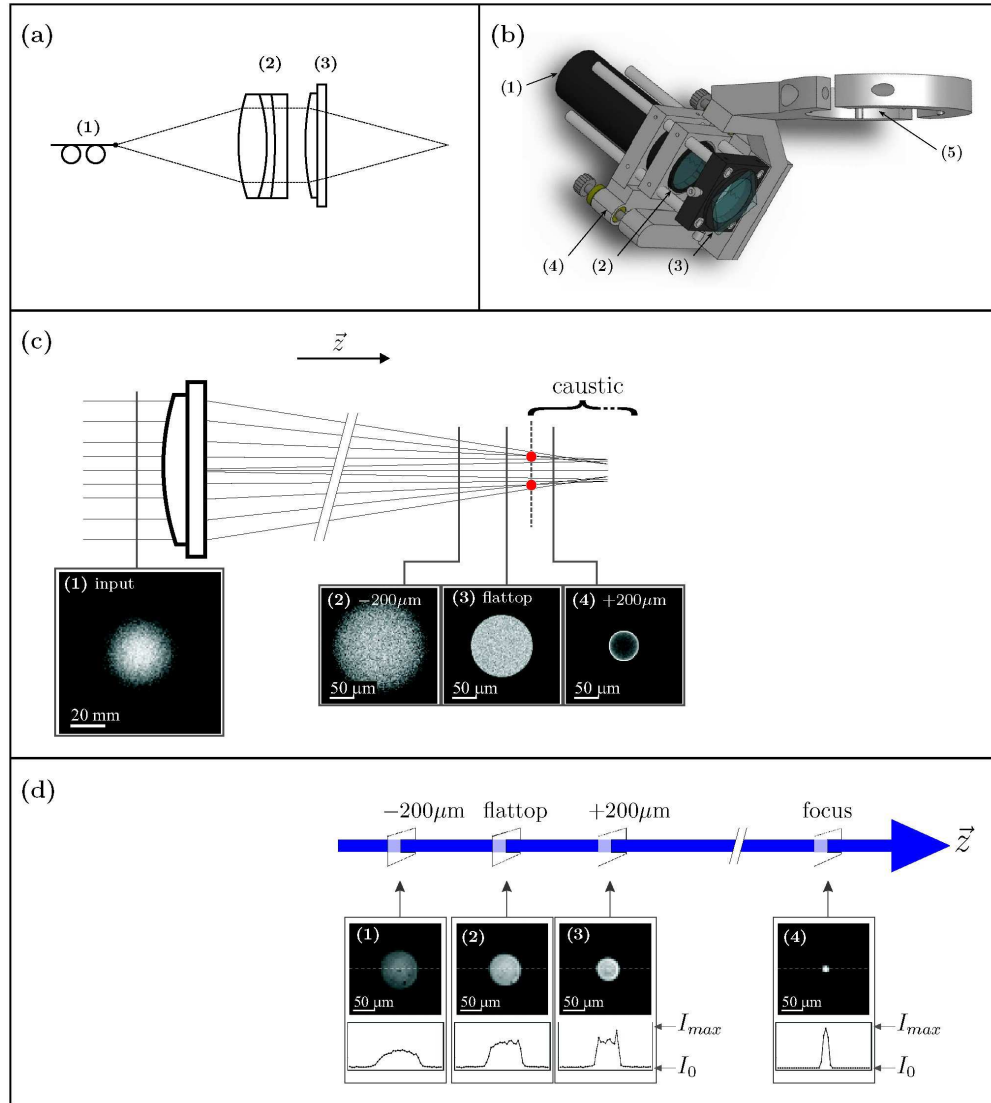


Figure 3. Realisation of a flattop beam profile for the 480 nm excitation laser. **(a)** Schematic: The output of a single-mode polarisation-maintaining fibre (1) is collimated by an achromat to a $1/e^2$ -intensity radius of 6.9 mm. The beam is focussed and shaped by a diffractive optical element which is cemented onto a standard plano-convex lens (3). **(b)** Supporting cage with (1) fibre connector, (2) achromat, and (3) diffractive element which is mounted on a 2-axes translation stage shown in black. The cage is fixed on an adapted 3-axes mirror mount (4) which is fixed to the vacuum chamber (5). **(c)** Beam shaping principle with ray optics. The collimated input beam (1) is focussed and shaped into a flattop beam profile at one specific distance (3). Before this region the shape is closer to a Gaussian beam (2), behind this point crossing rays (caustics) cause an increased intensity in the beam edges. **(d)** Measured beam profiles: (2) best resemblance of a flattop, (1) and (3) profiles at a distance of $200 \mu\text{m}$ from the flattop. The actual focus (4) is $640 \mu\text{m}$ further along the beam and is used for alignment (see Section 2.2). Figs. c.(4) and d.(3) show a difference between the designed and realized intensity distribution. The discrepancy is a consequence of imperfections in the actual setup, *e.g.* slight misalignment, inaccurate diameter of input beam, imperfect diffractive element.

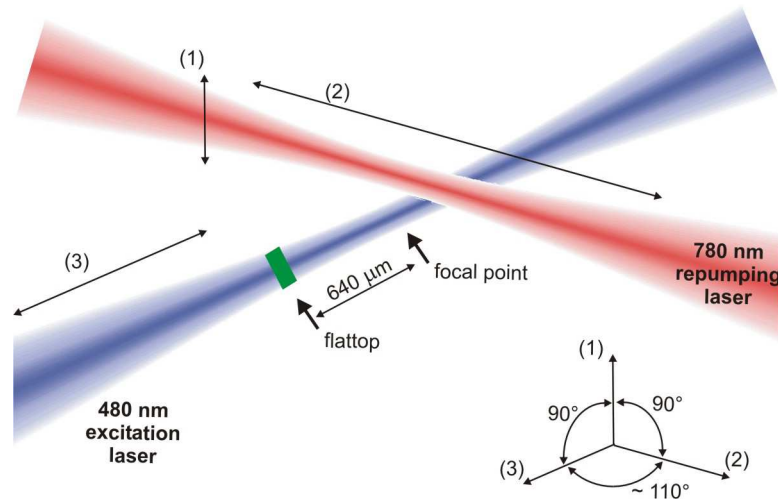


Figure 4. The excitation volume is given by the overlap region of a tightly focussed repumping beam (red) and the shaped 480 nm beam (blue). The lasers are aligned by first overlapping both foci (minimising the excitation volume) and then moving the flattop region onto the red beam by moving the blue focus by $640 \mu\text{m}$ along the beam direction (see Fig. 3(d)). Details see text.

which leads to an increased intensity at the beam edges. Even further along the beam is the actual focus.

We have aligned the elements within the cage by adjusting the distance between fibre output and achromat as well as the position of the DOE with respect to the centre of the collimated beam, and characterised the beam shape with a USB webcam (Philips ToUCam Pro PCVC740K). The CCD chip has been replaced by a black-and-white version (ICX098BL) with the protective glass cover removed and we have modified the firmware (WcRmac, v1.0.79, 2005, <http://www.astrosurf.com/astrobond/ebrawe.htm>). In this way we obtain raw, uncompressed, and unprocessed images at the full spatial resolution of the CCD chip ($5.6 \mu\text{m}$). The actual performance of the DOE as well as the closest approximation to a flattop is depicted in Fig. 3.(d). It is realised at a distance of $640 \mu\text{m}$ in front of the focal point.

2.2. Beam alignment: Selection of a mesoscopic subensemble

The previous characterisation of the shaped beam allows us to confine the excitation volume to the flattop region with a dedicated optical pumping scheme: The magnetic field of the MOT is turned off 3 ms before the trapping lasers are switched off and all atoms are pumped to the dark $|5S_{1/2}, F = 1\rangle$ ground state within $300 \mu\text{s}$ by a depumping laser (see Fig. 2). All atoms in a small cylindrical tube perpendicular to the excitation beams are transferred to the upper hyperfine component $|5S_{1/2}, F = 2\rangle$ of the ground state with a $1 \mu\text{s}$ pulse of a tightly focussed repumping beam (waist $10 \mu\text{m}$, power 10nW). All atoms in this tube are optically pumped to the stretched “launch” state

$|5S_{1/2}, F = 2, m_F = 2\rangle$ by a $1\mu\text{s}$ pulse of a σ^+ -polarised pumper beam superimposed with the 780 nm excitation laser. A small guiding field of 35 mG along the axis of the excitation lasers is turned on at all times. A sketch of the laser beam geometry is shown in Figure 1. Finally the atoms in the “launch” state are excited into Rydberg states. The excitation volume is therefore given by the overlap between the 480 nm laser and the repumping laser. This allows us to align the lasers by first overlapping both foci (minimising the excitation volume) and then moving the repumping beam onto the flattop in the following way (see Fig. 4):

The red beam is produced from the output of a single-mode fibre with a mounting that allows alignment along the directions (1) and (2). After a rough alignment the focus of the repumping beam is moved slightly above the blue beam by a small separation in direction (1). Moving the focus along direction (2) we only get an overlap with the 480 nm beam (and thus a Rydberg signal), when the divergence of the repumping beam is larger than the beam separation. In this way we can probe the Rayleigh-range of the red laser and thus find its focal point. After this we can measure the local width of the blue beam by moving the red laser along direction (1). As the mounting of the 480 nm beam allows movement of its focus along direction (3), we measure the 480 nm beam diameter in this way at several positions along direction (3) and thus overlap the 480 nm beam focus with the red beam. Finally we move the flattop region onto the red beam by moving the blue focus by $640\mu\text{m}$ along the beam direction (see Fig. 3(d)). We estimate an alignment accuracy of $50\mu\text{m}$ in direction (3) and an accuracy on the order of $10\mu\text{m}$ in direction (1). The excitation volume is given by the beam diameters resulting in a volume of about $10\mu\text{m} \times 10\mu\text{m} \times 100\mu\text{m}$ which (at our density of 10^{10}cm^{-3}) corresponds to 100 atoms in the excitation volume.

2.3. Background suppression

As our excitation volume is defined by the overlap of the repumping and the 480 nm beam (see Fig. 1), we can determine a background signal by blocking the repumping beam. The inset of Fig. 5 shows the spectral dependence of both the background signal (red) and the signal from the flattop region (green) on the detuning Δ of the 480 nm laser. The detuning of the 780 nm laser from the intermediate $5P_{3/2}, F = 3$ state is fixed at $\delta = +2\pi \times 110\text{MHz}$. The signal from the flattop region peaks at $\Delta \cong -\delta$, *i.e.* the two-photon resonance condition is fulfilled, which is the signature of coherent excitation [23]. By contrast, the background signal peaks at a different detuning. Fig. 5 shows the dependence of the peak positions for different values of δ . The spectral dependence shows that the background signal comes from the hot background gas from which the cold cloud is loaded: Due to their thermal velocity hot atoms experience the excitation lasers at their Doppler-shifted frequency. For atoms with a projected velocity v in the direction of the 780 nm laser, this laser is resonant with the transition $5S_{1/2} \rightarrow 5P_{3/2}$ if the Doppler shift $-2\pi \times v\lambda$ is equal to δ , with $\lambda = 780\text{nm}$ being the laser wavelength. As the two excitation lasers are counter-propagating these atoms are

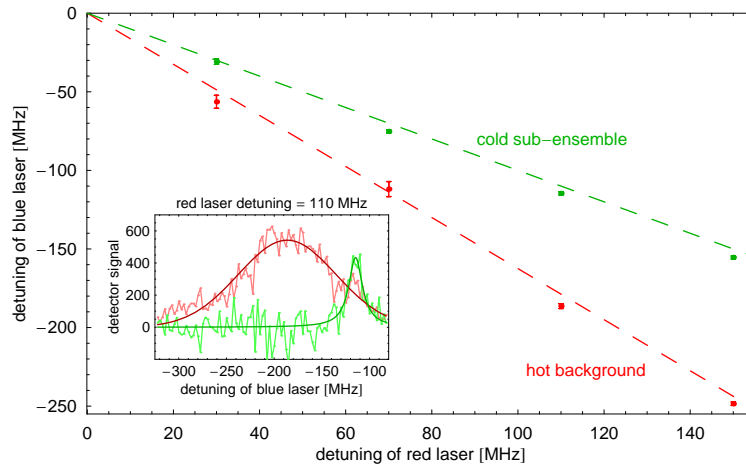


Figure 5. (Inset) Spectral dependence of both the background signal determined with a blocked repumping beam (red, with Gaussian fit) and the signal from the mesoscopic sample (green, with Lorentzian fit, background already subtracted) for a detuning of $\delta = 2\pi \times 110$ MHz from the intermediate level (see Fig. 2). For the detunings used in this article the background signal is usually between one tenth and one half the size of the signal from the mesoscopic cold ensemble. (Main graph) Peak position for the background signal (red dots) for different values of δ together with the peak position of the mesoscopic signal (green dots). The dashed green line shows the expected dependence for a coherent two-photon excitation, the dashed red line corresponds to the expectation for a hot gas as given by Eq. (1). Where error bars are not visible they are smaller than the dot size.

then resonant with the 480 nm laser if it is detuned from the resonance by

$$\Delta = 2\pi \times \frac{v}{480 \text{ nm}} = -\frac{780 \text{ nm}}{480 \text{ nm}} \delta. \quad (1)$$

The dashed red line in Fig. 5 shows this dependence in good agreement with the experimental values for the background spectra.

In this way the thermal velocity can be used to separate the signal from the hot atoms spectroscopically from the signal of the cooled atoms in the flattop excitation volume. We reduce the background even further by delaying the detection: After each excitation we wait for $30 \mu\text{s}$ before detection. In this time most of the hot atoms have already left the detection region which allows for a significant background suppression. Longer delays are not possible as the lifetime of the states discussed here are of the same order (*e.g.* $26 \mu\text{s}$ for 35D).

All figures shown in this article have been acquired by subtracting the background of hot atoms, which is determined by repeating the corresponding measurement with a blocked repumping beam.

2.4. Observation of Rabi oscillations

Our excitation scheme allows to excite either nS or nD states (n denotes the principal quantum number) depending on the helicity of the polarisation: We excite atoms to nS

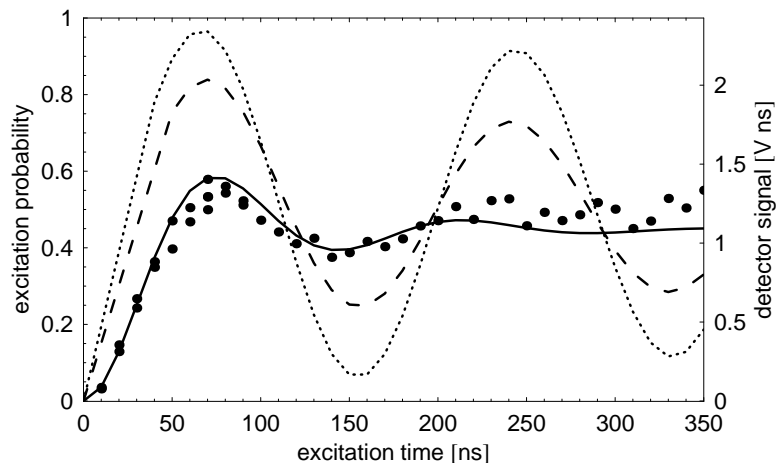


Figure 6. Rabi oscillations of atoms excited to the $31D_{5/2}$ state at a detuning from the intermediate state of $\delta/2\pi = 140$ MHz and a Rabi frequency for the lower transition of $\omega/2\pi = 55$ MHz. Each dot corresponds to an average of measurements over 28 experimental repetition cycles. The dotted line is the simulated excitation probability for a perfect flattop, *i.e.* a single Rabi frequency. In this case the damping comes from a small but finite admixture of the short-lived intermediate $5P_{3/2}$ state (see Sec. 3.4). The dashed line shows a simulation that additionally averages over the measured intensity distribution. Finally the solid line also takes an effective laser linewidth of 2.4 MHz into account. The MCP signal is given in V ns, and the axis is scaled to overlap with the simulated curve. The scaling factor constitutes the detector efficiency measured in mV ns per atom. The only free parameter for the simulations is the Rabi frequency for the upper transition which is compared to ab-initio calculations in Sec. 3.2.

states via

$$|5S_{1/2}, F = 2, m_F = 2\rangle \xrightarrow{\sigma^+} |5P_{3/2}, F = 3, m_F = 3\rangle \xrightarrow{\sigma^-} |nS_{1/2}, m_J = 1/2\rangle$$

and nD states via

$$|5S_{1/2}, F = 2, m_F = 2\rangle \xrightarrow{\sigma^+} |5P_{3/2}, F = 3, m_F = 3\rangle \xrightarrow{\sigma^+} |nD_{5/2}, m_J = 5/2\rangle$$

as depicted in Fig. 2.‡

In Fig. 6 the measured fraction of excited Rydberg atoms in the $31D_{5/2}$ state as a function of excitation time is shown. The excitation time is given by the pulse length of the 480 nm laser, as the 780 nm light is switched on (off) 100 ns before (after) the 480 nm laser to ensure constant intensity during the on-time of the latter. Fig. 6 shows a measured Rabi oscillation. It is damped out quickly. For times larger than 200 ns the number of Rydberg atoms reaches a steady state which indicates the balance between excitation and down-stimulation. The same temporal dependence is observed for nS and nD states with $n \lesssim 40$. For these small n it does not depend on the atom density. This indicates that the observed Rabi oscillations are not affected by

‡ Note that $|5P_{3/2}, F = 3, m_F = 3\rangle = |5P_{3/2}, I = 3/2, m_I = 3/2, m_J = 3/2\rangle$.

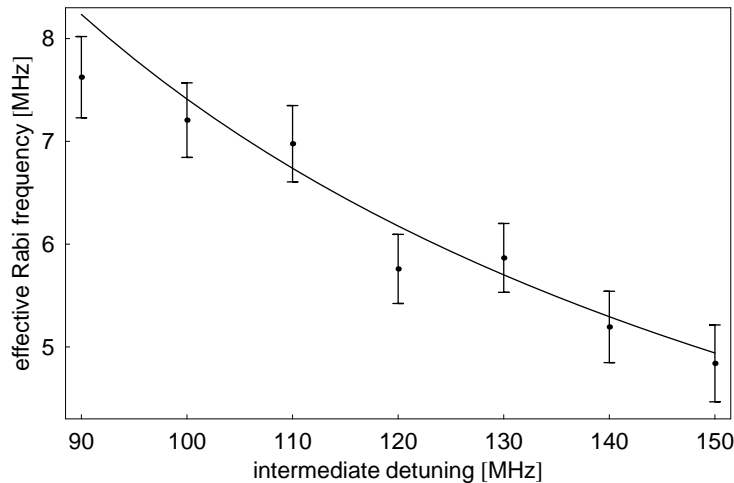


Figure 7. Measured effective Rabi frequencies $\Omega_{\text{eff}} / 2\pi$ for different detunings $\delta / 2\pi$ from the intermediate state. The solid line shows the theoretical prediction for a blue Rabi frequency $\Omega / 2\pi = 27$ MHz and a red Rabi frequency $\omega / 2\pi = 55$ MHz as deduced from an Autler-Townes splitting.

Rydberg–Rydberg interactions and that all atoms simultaneously perform identical Rabi oscillations. As seen in Fig. 6 the oscillations are strongly damped, which is a result of the remaining admixture of the intermediate state, the residual intensity distribution of the flat-top beam profile, and our finite laser bandwidth. We will discuss these sources for decoherence in Section 3.4.

3. Systematics

3.1. Dependence on the detuning from the intermediate state

If the detuning from the intermediate level is sufficiently large, one can reduce the actual three-level system to a two-level system with an effective Rabi frequency of $\Omega_{\text{eff}} = \omega \Omega / 2\delta$ where ω (Ω) denotes the Rabi frequency of the lower (upper) transition and δ denotes the detuning from the intermediate level. We have verified this dependence by measuring the effective Rabi frequencies for different detunings from the intermediate level. The effective Rabi frequencies are determined by a fit of a damped oscillation, $\frac{1}{2} [1 - \exp(-t/\tau_{\text{damp}}) \cos(\Omega_{\text{eff}} t)]$, $\tau_{\text{damp}} = 60$ ns, to measured Rabi oscillations. The resulting fit values together with the fit uncertainties are depicted in Fig. 7. They are in very good agreement with the expectation for an effective two-level system.

3.2. Comparison to ab-initio transition matrix elements

The experimental values of the Rabi frequencies are compared to ab-initio calculations yielding a concise test of predicted transition matrix elements. The Rabi frequency scales with the blue laser intensity I as $\Omega \propto \mu \sqrt{I}$ where μ is the matrix element between the states coupled by the laser light, *i.e.* the $5P_{3/2}$ and the Rydberg state.

Table 1. Comparison between measured Rabi frequencies and calculations based on ab-initio transition matrix elements.

final state	$\Omega_{\text{exp}} / 2\pi$	$\Omega_{\text{theo}} / 2\pi$
30D _{5/2}	32.8 ± 1.7 MHz	37.6 MHz
31S _{1/2}	18.9 ± 0.6 MHz	19.3 MHz

To determine μ we split the Rydberg electron wavefunctions $\psi_{n\ell j m_j}$ into a radial and a spherical part with the ansatz

$$\psi_{n\ell j m_j} = \sum_{m_s} \frac{1}{r} U_{n\ell j}(r) Y_{\ell m_j - m_s}(\theta, \varphi) C_{\ell, m_j - m_s, \frac{1}{2}, m_s}^{j, m_j} \Theta_{m_s}^{1/2}, \quad (2)$$

where $Y_{\ell m_\ell}$ denote the well-known spherical harmonics, $C_{\ell, m_j - m_s, \frac{1}{2}, m_s}^{j, m_j}$ is the Clebsch-Gordan coefficient and $\Theta_{m_s}^{1/2}$ is the spin wavefunction. The radial part is obtained by numerically integrating the Schrödinger equation with the Numerov algorithm following Ref. [28] at the energy $E_{n\ell j}$ (calculated with the according quantum defect). To obtain reasonable results for low-lying levels we use a model potential that is fitted to one-electron energies [29]. The knowledge of the radial wavefunctions allows us to calculate the radial part μ_{rad} of the dipole transition matrix element $\mu = \mu_{\text{rad}} \times \mu_{\text{sph}}$ with

$$\mu_{\text{rad}} = \left\langle \frac{1}{r} U_{5,P,3/2} \left| er \right| \frac{1}{r} U_{n,\ell,j} \right\rangle. \quad (3)$$

For large principal quantum numbers it scales as $\mu_{\text{rad}} \simeq C_\ell (n^*)^{-3/2}$, where n^* denotes the principal quantum number reduced by the appropriate quantum defect. For $n \geq 30$ we find $C_0 = 4.508$ a.u. and $C_2 = 8.475$ a.u. while the spherical matrix elements for the stretched transitions as depicted in Fig. 2 are $\mu_{\text{sph}} = \sqrt{1/3}$ for $\ell = 0$ (S) and $\sqrt{2/5}$ for $\ell = 2$ (D). Table 1 shows the comparison between the experimental values and the theoretical prediction. While there is excellent agreement for the 31S state, the measured value for the 30D state is slightly smaller than expected. The deviation is most likely caused by electric stray fields which induce an admixture of other m_j -states effectively reducing the spherical matrix element. This effect does not perturb the S_{1/2} state as $m_j = 1/2$ is the only dipole coupled state and the Stark effect on the intermediate 5P_{3/2} state is negligible.

3.3. Redistribution to other states

Redistribution of Rydberg atoms to other states due to population transfer processes has already been observed to reduce the efficiency of de-excitation (quenching) in a macroscopic cloud of Rydberg atoms [22]. By measuring the quenching for the 32S_{1/2} state as shown in Fig. 8 this process can be ruled out for the small mesoscopic ensemble described here. After 150 ns of excitation the 780 nm laser is turned off, while the laser for the upper transition is left on. Due to the short lifetime of the intermediate 5P_{3/2} state, population inversion is created. The blue laser stimulates transitions of the

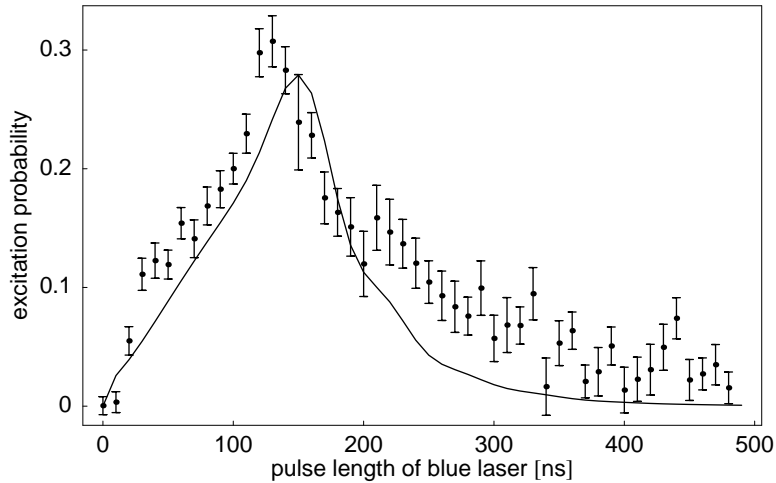


Figure 8. Quenching of Rydberg atoms by stimulated emission. At 150 ns, the laser at 780 nm for the lower transition is turned off, and Rydberg atoms in the $32S_{1/2}$ are stimulated to the $5P_{3/2}$ state by the laser light at 480 nm. Experimental values of the total Rydberg excitation with the corresponding statistical error are shown as dots. The solid line shows the excitation probability of the $32S_{1/2}$ state as predicted by a model calculation with no free parameters. The scaling factor for the MCP signal was determined by comparing the corresponding Rabi oscillation to a simulated curve as in Fig. 6.

Rydberg state to the intermediate state, which then quickly decays to the ground state. Redistribution processes would lead to population in other Rydberg states which are not coupled by the blue laser light. As these atoms are still field ionised, they should result in a finite MCP signal even for long quenching times. As Fig. 8 shows, the total number of Rydberg atoms is almost fully quenched by stimulated emission. In addition, the temporal evolution of the Rydberg signal is in good agreement with the solution of the Bloch equations for a pure three-level system shown as a solid line. Redistribution of Rydberg population can therefore be ruled out as a major cause of decoherence in the mesoscopic ensemble.

3.4. Sources for decoherence

Besides redistribution of Rydberg atoms to other states, three factors cause the reduced contrast and the damping of Rabi oscillations: the residual inhomogeneity of the flat-top intensity profile, the small but finite admixture of the short-lived intermediate $5P_{3/2}$ state, and the finite linewidth of the laser source. Note that only the last two effects are sources of decoherence for all atoms while the first effect only represents ensemble averaging with full coherence for each individual atom.

The influence of the intermediate state and the residual intensity distribution on the damping of the Rabi oscillations are simulated by solving the optical Bloch equations (OBE) for the 3-level system and averaging over different blue Rabi frequencies according to the measured intensity distribution shown in Fig. 2. The only free parameters are the

detection efficiency of the MCP and the average Rabi frequency of the upper transition, which agrees well with theory (see Section 3.2). The resulting simulations are depicted as dotted and dashed lines in Fig. 6 showing damped Rabi oscillations with reduced contrast. The dotted line is a simulation for a single Rabi frequency and shows a reduced contrast due to the admixture of the intermediate state which can be decreased by increasing the detuning δ which in turn results in a smaller effective Rabi frequency. The dashed line additionally incorporates an averaging over different Rabi frequencies corresponding to the measured residual intensity fluctuation in the flattop beam profile. The inhomogeneous distribution of Rabi frequencies alone does not fully explain the reduced measured contrast.

Indeed the main contribution to the reduced contrast is the finite bandwidth of the laser sources. As the admixture of the intermediate level is small we can incorporate the laser bandwidth γ into the simulation by solving the optical Bloch equation for a two-level system with a linewidth of γ and an effective Rabi frequency of $\Omega_{\text{eff}} = \omega \Omega / 2\delta$ where ω (Ω) denotes the Rabi frequency of the lower (upper) transition and δ denotes the detuning from the intermediate level. This is a good approximation for $\delta \gg \omega, \Omega$ [30]. We have again averaged over the different values of Ω_{eff} as present in the imperfect flat top. The corresponding model calculation for an effective incoherent excitation bandwidth of $\gamma = 2\pi \times 2.4$ MHz is shown as a solid line in Fig. 6 in excellent agreement with the experimental data. The experimental value for $\gamma/(2\pi)$ agrees well with the specified bandwidths of 2 MHz for the blue and 1 MHz for the red excitation laser. In addition we have performed beating measurements with two comparable, independent lasers at 780 nm which yielded a combined bandwidth of 2 MHz, in good agreement with the above values.

4. Van der Waals blockade

The excitation presented so far has been performed in a regime with negligible interactions at small n . For large values of $n \gtrsim 60$ we do not observe Rabi oscillations as the Rabi frequency, scaling with $n^{-3/2}$ becomes smaller than the dephasing rate. On the other hand these higher lying states exhibit stronger Rydberg-Rydberg interactions which can result for example in a van der Waals blockade. Fig. 9(c) shows how the excitation probability of the 75S state depends on the ground state density. For a single (or non-interacting) atom we can solve the optical Bloch equation for the independently determined experimental parameters and obtain a value represented by the dashed line. For low densities the measured excitation probability agrees well with the prediction. With increasing density we observe an increasing suppression of the excitation probability. It is accompanied by a significant line broadening which is shown as inset in Fig. 9(d) as well as in the exemplary spectra in Fig. 9(a) and (b). For small densities the measured linewidth agrees well with a convolution of our laser bandwidth (2.4 MHz) and saturation broadening (1.7 MHz).

The suppression of excitation marks the onset of the dipole blockade. The

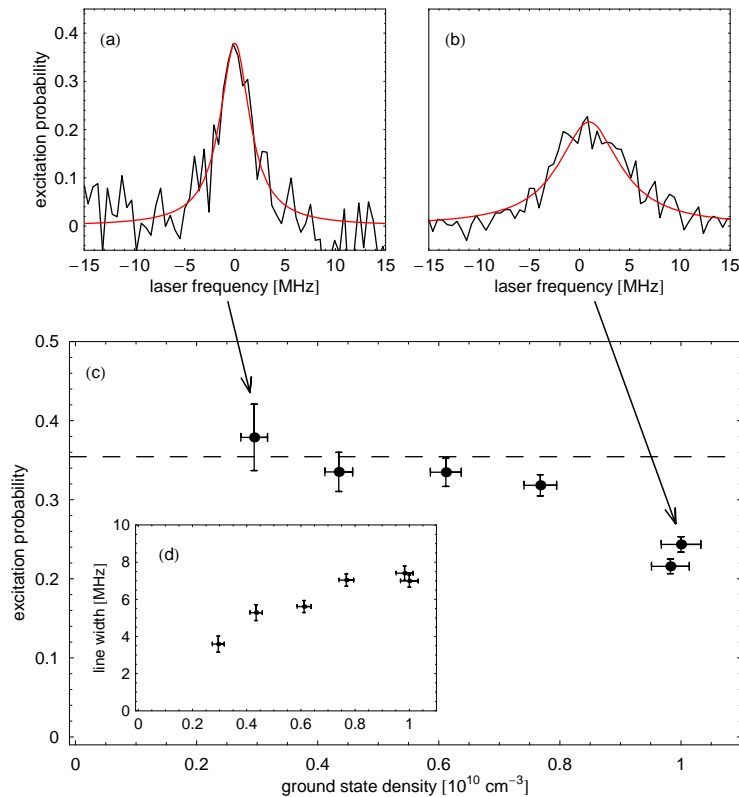


Figure 9. Excitation blockade for a mesoscopic ensemble of atoms in the 75S state. The upper graphs show excitation spectra for the highest (a) and lowest (b) investigated densities together with Lorentzian fits. The higher density is clearly accompanied by smaller excitation probability and a significant line broadening. The excitation probabilities are calibrated by measurements at low n , which results in single atom excitation probabilities. (a) shows the maximum excitation for different ground state densities. The dashed line corresponds to the theoretical excitation probability for non-interacting atoms. For higher densities the Rydberg-Rydberg interaction energy rises and moves the excitation out of resonance reducing the excitation probability on resonance. The corresponding line broadening (shown in (d) with an identical x-axis) also reflects the increasing interaction energy.

underlying interaction has van der Waals character with a C_6/R^6 dependence on the interatomic spacing R in contrast to dipole-dipole interaction with R^{-3} character, which was originally proposed [3]. In comparison this means a shorter interaction range and in fact we see the suppression due to vdW interaction only for high principal quantum numbers n as the vdW coefficient scales as $C_6 \propto n^{11}$.

These results complement our earlier measurements with macroscopic atom clouds [17] which showed a much stronger broadening at comparable densities and excitation suppression. In fact the observed broadening in the macroscopic cloud cannot be explained by mere Rydberg-Rydberg interactions [31]. One possible explanation may be ions that are produced by interaction-induced collisions between the cold atoms after acceleration by the strong van der Waals forces between Rydberg atoms [32, 33]. For the

mesoscopic system investigated here we have ruled out the presence of ions directly by selective field ionisation. This is also expected for the small number of involved atoms and the short excitation times.

5. Conclusion

We have observed Rabi oscillations of a mesoscopic cloud of about 100 atoms in the coherent excitation of Rydberg states out of an ultracold atom cloud. The reduced contrast of the Rabi oscillation is traced back to residual intensity variations and the finite bandwidth of our laser system. While the latter can simply be solved improving the frequency stability of the laser systems, one option to bypass the first limitation is the use of liquid crystal elements [34] to dynamically optimise the diffractive pattern for better results.

In addition we have demonstrated the van der Waals blockade at large principal quantum numbers for a mesoscopic cloud. This indicates the onset of a local blockade as has been observed before for macroscopic clouds [16, 17, 20, 18, 19, 21]. The full blockade regime can be identified by an increased Rabi frequency $\sqrt{N}\Omega$, where N and Ω denote the number of atoms and the atomic Rabi frequency, respectively [3]. The experiments presented here constitute a necessary prerequisite for the direct observation of this coherent many-body phenomenon. In future work we will use a number of options to reach this regime by increasing the interaction strength through higher densities [21] and using either resonant [18] or permanent [19] dipole-dipole interactions. Smaller excitation volumes [24] will provide ensembles where even the interaction between the farthest separated atoms dominates all other energy scales.

Acknowledgments

We thank C. Pruss and W. Osten from the Institute for Technical Optics at the University of Stuttgart for the design and production of the beam shaping element. The project is supported by the Landesstiftung Baden-Württemberg within the "Quantum Information Processing" programme, and by a grant from the Ministry of Science, Research and Arts of Baden-Württemberg (Az: 24-7532.23-11-11/1).

References

- [1] T. F. Gallagher. *Rydberg Atoms*. Cambridge University Press, Cambridge, 1994.
- [2] D. Jaksch, J. I. Cirac, P. Zoller, S. L. Rolston, R. Côté, and M.D. Lukin. Fast quantum gates for neutral atoms. *Phys. Rev. Lett.*, 85:2208, 2000.
- [3] M. D. Lukin, M. Fleischhauer, R. Côté, L. M. Duan, D. Jaksch, J.I. Cirac, and P. Zoller. Dipole blockade and quantum information processing in mesoscopic atomic ensembles. *Phys. Rev. Lett.*, 87:037901, 2001.
- [4] Y. Miroshnychenko, W. Alt, I. Dotsenko, L. Förster, M. Khudaverdyan, D. Meschede, D. Schrader, and A. Rauschenbeutel. Quantum engineering: An atom-sorting machine. *Nature*, 442:151, 2006.

- [5] M. Cozzini, T. Calarco, A. Recati, and P. Zoller. Fast rydberg gates without dipole blockade via quantum control. *Opt. Comm.*, 264:375, 2006.
- [6] D. Bouwmeester, A. Ekert, and A. Zeilinger (eds.). *The Physics of Quantum Information*. Springer, Berlin, 2000.
- [7] M. A. Nielsen and I. L. Chuang. *Quantum Computation and Quantum Information*. Cambridge University Press, Cambridge, 2000.
- [8] P. Treutlein, P. Hommelhoff, T. Steinmetz, T. W. Hänsch, and J. Reichel. Coherence in microchip traps. *Phys. Rev. Lett.*, 92:203005, 2004.
- [9] Q. A. Turchette, C. J. Hood, W. Lange, H. Mabuchi, and H. J. Kimble. Measurement of conditional phase shifts for quantum logic. *Phys. Rev. Lett.*, 75:4710, 1995.
- [10] D. Jaksch, H.-J. Briegel, J. I. Cirac, C. W. Gardiner, and P. Zoller. Entanglement of atoms via cold controlled collisions. *Phys. Rev. Lett.*, 82:1975, 1999.
- [11] W. R. Anderson, J. R. Veale, and T. F. Gallagher. Resonant dipole-dipole energy transfer in a nearly frozen rydberg gas. *Phys. Rev. Lett.*, 80:249, 1998.
- [12] I. Mourachko, D. Comparat, F. de Tomasi, A. Fioretti, P. Nosbaum, V.M. Akulin, and P. Pillet. Many-body effects in a frozen Rydberg gas. *Phys. Rev. Lett.*, 80:253, 1998.
- [13] W. R. Anderson, M. P. Robinson, J. D. D. Martin, and T. F. Gallagher. Dephasing of resonant energy transfer in a cold Rydberg gas. *Phys. Rev. A*, 65:063404, 2002.
- [14] M. Mudrich, N. Zahzam, T. Vogt, D. Comparat, and P. Pillet. Back and forth transfer and coherent coupling in a cold rydberg dipole gas. *Phys. Rev. Lett.*, 95:233002, 2005.
- [15] S. Westermann, T. Amthor, A. L. de Oliveira, J. Deiglmayr, M. Reetz-Lamour, and M. Weidemüller. Dynamics of resonant energy transfer in a cold Rydberg gas. *Eur. Phys. J. D*, 40:37, 2006.
- [16] D. Tong, S. M. Farooqi, J. Stanojevic, S. Krishnan, Y.P. Zhang, R. Côté, E. E. Eyler, and P. L. Gould. Local blockade of Rydberg excitation in an ultracold gas. *Phys. Rev. Lett.*, 93:063001, 2004.
- [17] K. Singer, M. Reetz-Lamour, T. Amthor, L.G. Marcassa, and M. Weidemüller. Suppression of excitation and spectral broadening induced by interactions in a cold gas of rydberg atoms. *Phys. Rev. Lett.*, 93:163001, 2004.
- [18] T. Vogt, M. Viteau, J. Zhao, A. Choa, D. Comparat, and P. Pillet. Dipole blockade at Förster resonances in high resolution laser excitation of Rydberg states of cesium atoms. *Phys. Rev. Lett.*, 97:083003, 2006.
- [19] T. Vogt, M. Viteau, A. Chotia, J. Zhao, D. Comparat, and P. Pillet. *Phys. Rev. Lett.*, 99:073002, 2007.
- [20] T. Cubel Liebisch, A. Reinhard, P. R. Berman, and G. Raithel. Atom counting statistics in ensembles of interacting rydberg atoms. *Phys. Rev. Lett.*, 95:253002, 2005.
- [21] R. Heidemann, U. Raitzsch, V. Bendkowsky, B. Butscher, R. Löw, L. Santos, and T. Pfau. Evidence for coherent collective Rydberg excitation in the strong blockade regime. *Phys. Rev. Lett.*, 99:163601, 2007.
- [22] T. Cubel, B. K. Teo, V. S. Malinovsky, J. R. Guest, A. Reinhard, B. Knuffman, P. R. Berman, and G. Raithel. Coherent population transfer of ground-state atoms into Rydberg states. *Phys. Rev. A*, 72:023405, 2005.
- [23] J. Deiglmayr, M. Reetz-Lamour, T. Amthor, S. Westermann, K. Singer, A. L. de Oliveira, and M. Weidemüller. Coherent excitation of Rydberg atoms in an ultracold gas. *Opt. Comm.*, 264:293, 2006.
- [24] T. A. Johnson, E. Urban, T. Henage, L. Isenhower, D. D. Yavuz, T. G. Walker, and M. Saffman. Rabi flopping between ground and Rydberg states with dipole-dipole atomic interactions. *arXiv:0711.0401*, 2007.
- [25] M. Reetz-Lamour, J. Deiglmayr, T. Amthor, and M. Weidemüller. Rabi oscillations and excitation trapping in the coherent excitation of a mesoscopic frozen Rydberg gas. *arXiv:0711.4321*, 2007.
- [26] S. H. Autler and C. H. Townes. Stark effect in rapidly varying fields. *Phys. Rev.*, 100:703, 1955.

- [27] B. K. Teo, D. Feldbaum, T. Cubel, J. R. Guest, P. R. Berman, and G. Raithel. Autler-Townes spectroscopy of the $5S_{1/2}$ - $5P_{3/2}$ - $44D$ cascade of cold ^{85}Rb atoms. *Phys. Rev. A*, 68:053407, 2003.
- [28] M. L. Zimmerman, M. G. Littman, M. M. Kash, and D. Kleppner. Stark structure of the Rydberg states of alkali-metal atoms. *Phys. Rev. A*, 20:2251, 1979.
- [29] M. Marinescu. Dispersion coefficients for alkali-metal dimers. *Phys. Rev. A*, 49:982, 1994.
- [30] B.W. Shore. *The Theory of Coherent Atomic Excitation, Volume 2, Multilevel Atoms and Incoherence*. Wiley, New York, 1990.
- [31] C. Ates, T. Pohl, T. Pattard, and J. M. Rost. Many-body theory of excitation dynamics in an ultracold rydberg gas. *Phys. Rev. A*, 76:013413, 2007.
- [32] T. Amthor, M. Reetz-Lamour, S. Westermann, J. Denskat, and M. Weidemüller. Mechanical effect of van der Waals interactions observed in real time in an ultracold Rydberg gas. *Phys. Rev. Lett.*, 98:023004, 2007.
- [33] T. Amthor, M. Reetz-Lamour, C. Giese, and M. Weidemüller. Modeling many-particle mechanical effects of an interacting Rydberg gas. *Phys. Rev. A*, 76:054702, 2007.
- [34] S. Bergamini, B. Darquié, M. Jones, L. Jacubowicz, A. Browaeys, and P. Grangier. Holographic generation of microtrap arrays for single atoms by use of a programmable phase modulator. *J. Opt. Soc. Am. B*, 21:1889, 2004.